SIMULATION OF RESIDUAL STRESSES DURING THE WIRE ARC ADDITIVE MANUFACTURING (WAAM) PROCESS

A. A. ALRUMAYH*, H. F. NIED**

**Department of Mechanical Engineering, College of Engineering, Qassim University, Unaizah,, Saudi Arabia*
***Mechanical Engineering and Mechanics, Lehigh University, Bethlehem, PA 18015, USA*

DOI 10.3217/978-3-85125-968-1-15

ABSTRACT

This study examines the residual stresses and distortion that can occur during the Wire Arc Additive Manufacturing (WAAM) process. Of particular interest is the evolution of the residual stresses due to the repetitive heating and cooling associated with the moving arc heat source and deposition of hot metal during the layer-by-layer metal deposition process. The presented results show how the fundamental welding process parameters, thermomechanical material properties, and clamping/fixture conditions affect the post-processing residual stresses. For thin-walled structures, these residual stresses can result in significant warpage and/or premature cracking. This computational study is primarily based on the application of finite element models generated using the SYSWELD finite element software to simulate the coupled heat transfer and mechanical behavior during the layer-by-layer "printing" of a thin, 3-D rectangular plate. Of particular interest are the residual stress comparisons between an austenitic stainless steel, AISI 316L, and a low-carbon steel alloy, S355J2G3. The differences in residual stresses are closely related to the differences in the volumetric strains associated with the metallurgical phase changes between these two different steel alloys.

Keywords: Additive Manufacturing, WAAM, residual stresses, deformation, phase changes, isotropic hardness, heat treatment, size effects

INTRODUCTION

WAAM (Wire Arc Additive Manufacturing), is an effective Additive Manufacturing (AM) process that provides an economical technology path for fabricating large mechanical components [1-3]. The ability to build large load-bearing parts, in some cases up to a few meters in size [2], with significant geometric complexity [3], is particularly attractive for structural applications (Fig. 1). The two most frequently employed deposition techniques used in conventional WAAM processes are: Gas Metal-Arc Welding (GMAW) and Gas Tungsten-Arc Welding (GTAW). The energy efficiency of the electric arc can be as much as 90% in these welding processes.

Fig. 1 Sample WAAM structural components fabricated at Lehigh University's Additive Manufacturing Life Analysis Lab. Courtesy of Dr. C. Haden

Of particular significance for the fabrication of large metal parts is WAAM's capacity for high deposition rates, generally lower system and material costs, and a lower likelihood of oxide contamination [4-5]. For example, WAAM can attain deposition rates of 3–7.8 kg/h, whereas powder bed based systems usually only have deposition rates of 0.12–0.6 kg/h [6]. Typical metal alloys used in WAAM include: titanium and its alloys, steel, aluminum, and nickel alloys. It is well-known that wire fed AM systems generally provide relatively low resolution when compared with most powder-based deposition processes. Not only are the feed wire diameters considerably larger than the fine powder sizes available for powdered metals, but arc welding also introduces a larger melt pool size and relatively high post-weld distortion. The typical reported "precision" attained using WAAM is on the order of ±0.2 mm vs ±0.04 mm for powder-based systems. Thus, WAAM is generally not recommended for "printing" intricate parts with small length scale features [7-8].

WAAM processes can introduce very large residual stresses [9], which if not relieved can lead to undesirable distortion, especially in thin-walled parts. Since WAAM is based on well-understood direct fusion welding processes, conventional welding process parameters can be effectively utilized and controlled with little trial and error. The most important welding parameters are the arc voltage, arc current, shielding gas, nozzle-base distance, travel speed, wire feed speed, and wire diameter. These process parameters are known to most strongly influence the weld bead geometry, distortion, and resulting residual stresses [3]. The main issues encountered in WAAM are the same as those associated with all fusion welding processes, i.e., potential lack of fusion, porosity, vaporization, undesirable mechanical properties in the heat affected zone, grain structure, surface finish, deformation and distortions, high residual stresses, and cracking [10].

Fortunately, some of these issues are the result of reversible thermal effects and can be mediated by post-weld heat treatment. The quality of the weld bead profile is a common controllable issue and is caused by three main factors: layer thickness deviation, undercutting, and unsymmetrical weld beads [11-12]. WAAM welding residual stresses can result in distortions and/or cracking in the finished work piece.

During the AM deposition process, the sequentially deposited metal layers are repeatedly heated from the heat of other successively deposited bead layers. This introduces a complex thermal cycle for each layer [13]. Since WAAM is a high heat input process, the heat affected zone can be large and may lead to undesirable metallurgical changes that can contribute to localized cracking. If the thermal gradients are large enough, and the workpiece is highly constrained, the residual stresses can be quite high. Generally, the internal stresses are relieved to some degree when the work piece is unclamped, but this can result in undesirable warpage. Finally, it has been observed that the largest residual stress component is usually coincident with the direction of the deposition path [12].

As shown in Fig. 2, even a relatively simple build of a rectangular plate using WAAM can develop slight dimensional deviations that can propagate upwards through the build layers. Thus, minor defects in the build process tend to be amplified during the deposition of subsequent layers [6]. In addition, it has been observed that the last few layers in the AM deposition process exhibit higher hardness, because these layers experience fewer reheating cycles [14].

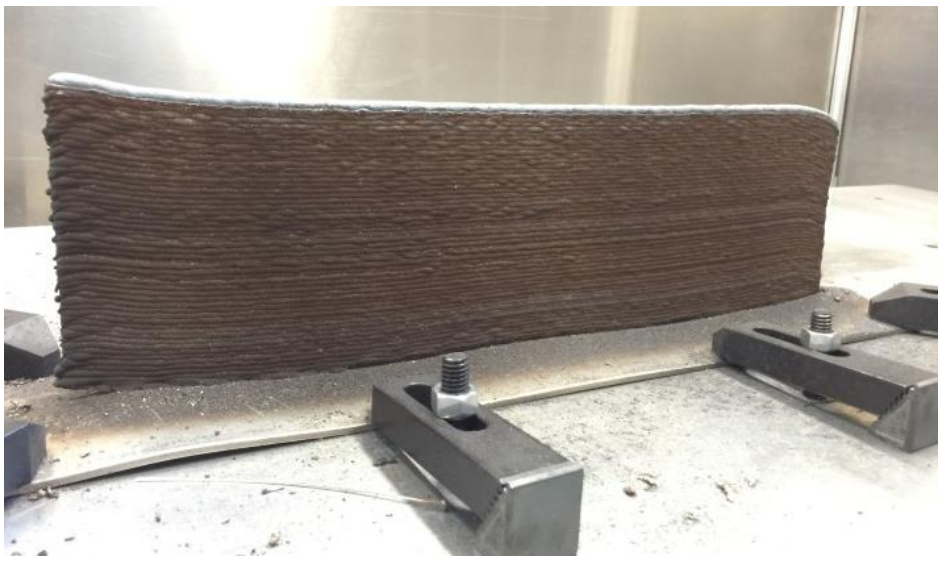

Fig. 2 WAAM build of a rectangular plate, in the clamped configuration, depicting the layer-by-layer macroscopic structure formation. Note the local lifting in the base plate, due to residual stresses. Lehigh University's Additive Manufacturing Life Analysis Lab. Courtesy of Dr. C. Haden

Various techniques have been explored to improve and control the build geometry, the residual stresses and metallurgical properties during WAAM processing. Some of the techniques that have been investigated for improving WAAM residual stresses and minimizing welding distortion include: preheating the substrate prior to deposition, selective secondary heating, spatial and temporal optimization of the weld path, and high-pressure rolling [14-22]. Because of the large number of controllable welding parameters, it is not particularly effective to rely solely on an experimental approach to optimize the quality of WAAM builds. It is recognized that computational simulations can greatly assist in the development of improved build processes based on well-established welding physics.

Because of the highly nonlinear thermomechanical behavior associated with welding deposition processes, FEA (finite element analysis) codes are the preferred computational tools for simulating transient heat transfer and residual stress evolution during welding. For welding process simulations, most general purpose, commercially available, software packages are usually adequate, but may be cumbersome to use for modeling specific welding processes. In this study, the authors used ESI's specialized FEA welding simulation software, SYSWELD [23], which provides built in tools that greatly simplify the input of welding process parameters that can be adequately characterized using a predefined moving heat source [24-26]. SYSWELD can also be used to obtain the phase proportions, hardness, distortions, residual stresses, and plastic strains distributions associated with post-weld heat treatment [27]. In order to systematically understand and improve WAAM process, it is desirable to accurately simulate multipass welding in detail using a variety of weld deposition paths and welding parameters. However, it's unlikely that a brute force modeling/simulation approach will be very effective for modeling complex AM builds, since the computational requirements needed to sequentially model the deposition of every single build layer in a complex build is well beyond current computational capabilities. Currently, it is feasible to perform computational simulations of multipass welding for a few hundred weld passes. However, the information obtained from "local" detail models can ultimately be used to develop more efficient global simulation models, where the local models form the basis, or building blocks, for global models that incorporate local temperatures, stresses and strains into the global model.

MODELLING DETAILS

The problem of interest in this study is the layer-by-layer WAAM build of a flat metal plate, as shown in Figs. 2 and 3. A number of these plates were fabricated at Lehigh University in a separate study to measure fatigue crack growth rates in stainless steel WAAM specimens cut from the plates shown [28]. During the fabrication of these plate specimens, it was noted that the residual stresses that were introduced during the build process were of sufficient magnitude to noticeably bend the 5 mm thick base plate, as shown in Fig. 3, upon release of the clamping fixtures.

Fig. 3 WAAM fabricated 304 stainless steel plate. Note the bending of the solid base plate after release from the clamping fixtures. Lehigh University's Additive Manufacturing Life Analysis Lab [28]

The computational simulations presented in this paper examine the differences in the evolution of the residual stress, displacements, hardness, and phase changes for two specific alloys: 1) 316L austenitic stainless steel, and 2) S355J2G3 low-carbon steel. The reason these specific steel alloys were selected, is because they exhibit markedly different phase change behaviors and their temperature dependent material properties have been accurately characterized and incorporated into the SYSWELD material property database. It is believed that these two steel alloys effectively demonstrate the fundamental difference in residual stress evolution between two broad classes of carbon steels and austenitic stainless steels of interest for many WAAM applications. Table 1 provides the chemical composition of the two alloys.

Table 1 Chemical composition of the steel alloys used in WAAM simulations

Element %	C	Cr	Mn	Mo	Ni	P	S	Si
AISI 316L	0.03	17	2	2.5	12	0.045	0.03	0.75
S355J2G3	0.18	-	1.6	-	-	0.035	0.035	0.55

The melting points are 1400°C for 316L, and 1500°C for S355J2G3. Fig. 4 depicts the Young's modulus for these alloys as a function of temperature.

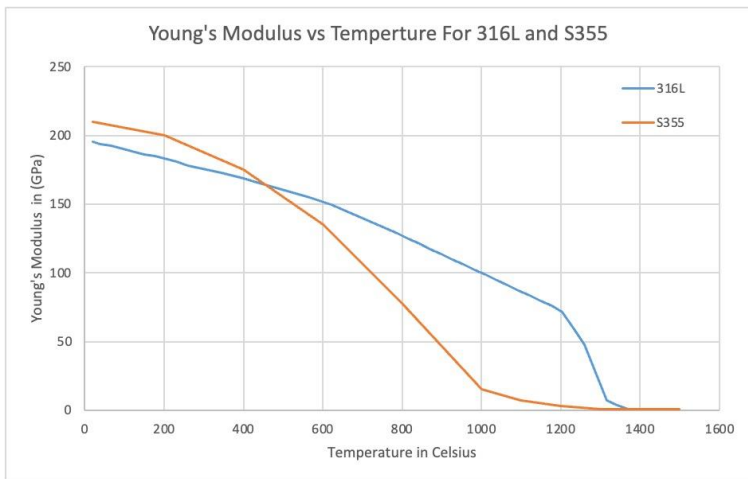

Fig. 4 Young's Modulus vs Temperature For 316L and S355

The other critical mechanical property that has a strong influence on the residual stress state is the temperature dependent yield strength depicted in Fig. 5. This figure shows the yield strength for 316L in one phase and for all six phases of the low-carbon steel S355J2G3. As can be seen in the figure, there is little difference between the nominal yield strengths above 800°C, while above 1300°C, the yield strengths (and stiffness) for both alloys are essentially zero for all material phases. Therefore, above 1300°C, any inaccuracies in the local moving heat source model will have little influence on the stress state. However, as post-weld cooling occurs, it is expected that there will be significant differences in the residual stresses between these two alloys as a function of temperature.

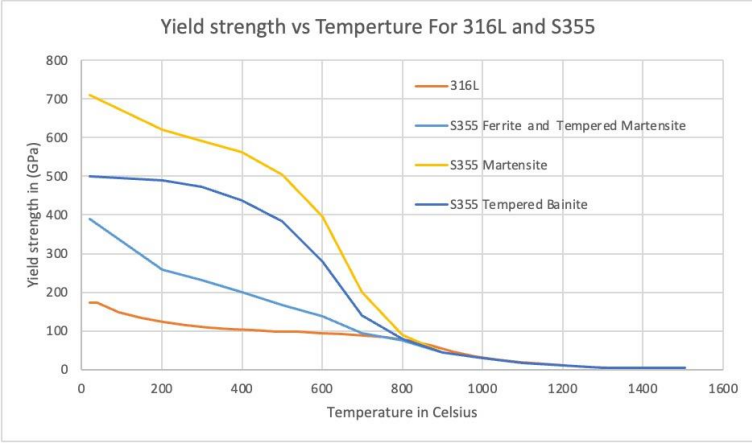

Fig. 5 Yield strength vs Temperature for 316L and S355J2G3

Table 2 gives the basic welding parameters used to compare AM builds for both of the steel alloys described above. Since the thermomechanical properties are different for these alloys, 316 L required a power input of 1015 W to form a satisfactory weld pool size, and 1265 W was used for the low-carbon steel S355J2G3 in order to obtain equivalent weld pool dimensions.

Table 2 WAAM simulation processes parameters in SYSWELD

WAAM parameters	316L	S355J2G3
Input power (Watts)	1015	1265
Substrate and Wire Material	Stainless-steel 316L	Low carbon steel S355J2G3
Welding speed (mm/s)	2.5	
Number of layers	38	
Layer length (mm)	700	
Layer Height (mm)	2.4	
Layer Thickness (mm)	8	
Substrate Dimension (mm)	5 X 100 X 855	

The simulated WAAM builds were patterned after the process variables and dimensions used in [28], to fabricate the plate shown in Fig. 3. A standard double

ellipsoid moving heat source was used to model the arc welding process. The path of the metal deposition was a unidirectional path, where the individual deposition sequences started at the leftmost end of the plate and ended at the rightmost end for each build layer. With the welding speed set at 2.5 mm per second, each layer took 280 seconds to complete. There was no time delay between the completion of one build layer and the start of the next.

Since the welding simulations in this study did not attempt to model the fluid mechanics, electromagnetic, and surface tension effects in the weld pool, it was necessary to "define" a priori the shape and dimensions of the weld pool and deposited metal geometry based on experimental measurements. For this study, cut sections were taken from samples generated in [28] to determine the shape of the individual weld bead layers. Printed plates were vertically cross-sectioned, ground, polished, and etched to clearly visualize the borders between each individual printed layer. Fig. 6 shows the actual printed cross section and the representative finite element mesh used in the numerical simulations. It is believed that the simplified cross-sectional geometry used for the numerical simulations, reasonably represents the printed cross section geometry in some average sense.

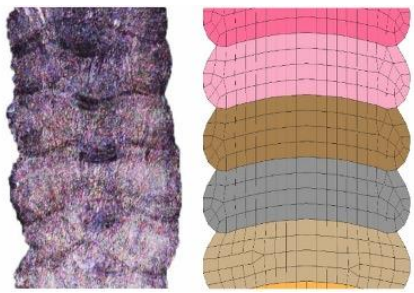

Fig. 6 Comparison between the experimentally generated layer cross-sections (left) and the finite element mesh used for the numerical models (right)

The ½ symmetry model shown in Fig. 7, was used to reduce computation times and to clearly visualize differences between the internal temperatures and stresses on the symmetry plane and the external surface. During the welding simulations, clamped boundary conditions, which prevented vertical (z) displacements, were specified on the corners and the mid-side of the substrate. The clamped areas are shown as red rectangular regions on the substrate surface in Fig. 7. After the workpiece cooled, the clamped boundary conditions were removed to obtain the final residual stresses and displaced configuration.

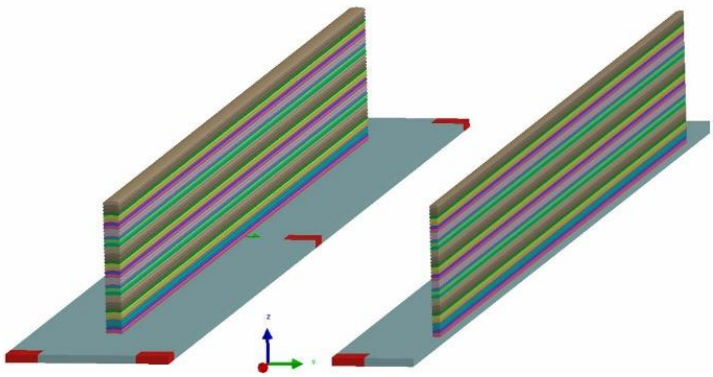

Fig. 7 Full 3-D model (left), symmetry model (right)

SIMULATION RESULTS

HEAT TRANSFER AND TEMPERATURES

In multipass welding, where layers of hot metal are deposited on top of previously deposited cooler metal, the dominant heat transfer mechanism is conduction through the metal layers. Some heat is lost through surface convection and radiant heat transfer, but these losses are relatively small during the actual welding process. In the development of the WAAM models, care was taken to ensure that temperatures in each newly deposited layer attained the designated melt temperature. Typically, 3 nodes in a newly deposited layer (shown in Fig. 8) were monitored during the welding simulations to ensure that melt temperatures were achieved in each deposited layer. The moving arc weld heat source was also defined in such a manner that sufficiently high temperatures were reached on the boundaries between adjacent layers to allow for interlayer fusion. This meant that the defined heat source's ellipsoidal boundary had to penetrate to a sufficient depth into a previously deposited layer.

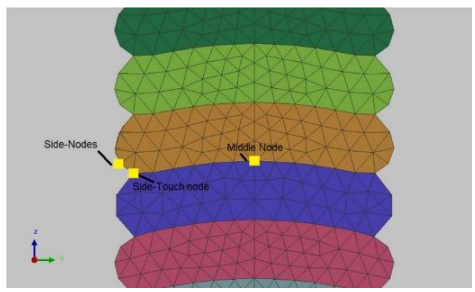

Fig. 8 Locations where temperatures were monitored to ensure bulk melting in each new layer

Fig. 9 shows the temperature history profiles, during the deposition of each layer at the nodes depicted in Fig. 8, for selected layers in the 316L stainless steel model. In general, the temperature history profile for each new layer is very similar to the temperatures observed in previous layers. As the build progresses, and subsequent layers are deposited, a new, lower temperature peak is observed in each of the previously deposited layers due to conduction effects. As the moving heat source increments upwards following the deposition of each new layer, the temperature peak gets smaller and smaller in the lower, previously deposited layers. In Fig. 9 it can be seen that for each layer, the melting point temperature of 1400ºC is exceeded twice at the center node on the lower weld interfaces. This is because it is the closet node to the moving heat source when the next layer is deposited. It's interesting to note that evidence of this secondary melting effect can be seen by the small dark regions depicted in the weld bead cross-sections shown in the left image in Fig. 6. Similar temperature history profiles are obtained for the low-carbon steel material model, S355J2G3, shown in Fig. 10. Because of the higher power input and higher melting point for the low-carbon steel, the temperatures at the monitored nodes initially exceed 1500° during the layer's deposition. But otherwise, the heat transfer behavior, i.e., repeated rapid heating and cooling is identical to the 316L behavior.

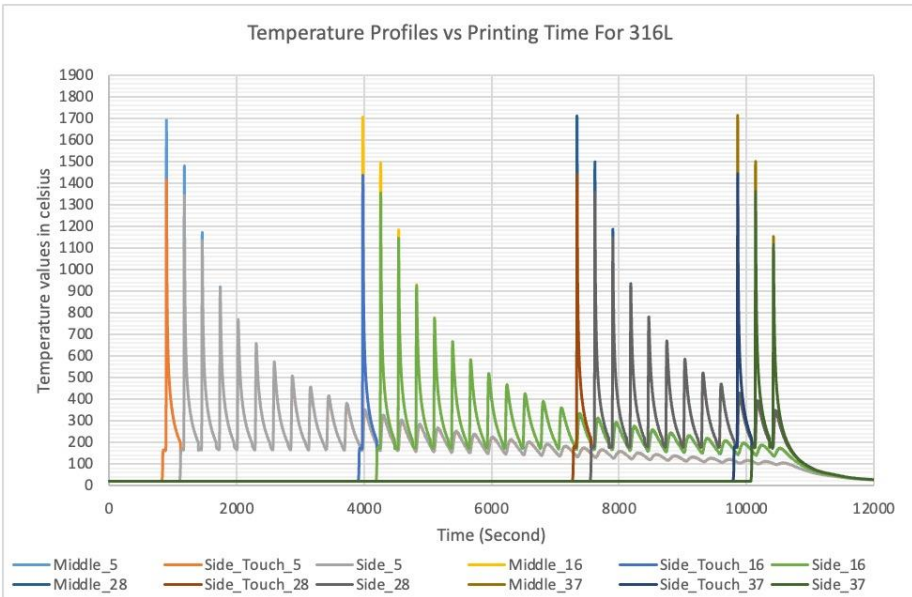

Fig. 9 Temperature history at specific points shown in Fig. 8 for layers 5, 16, 28, and 37 for 316L stainless steel

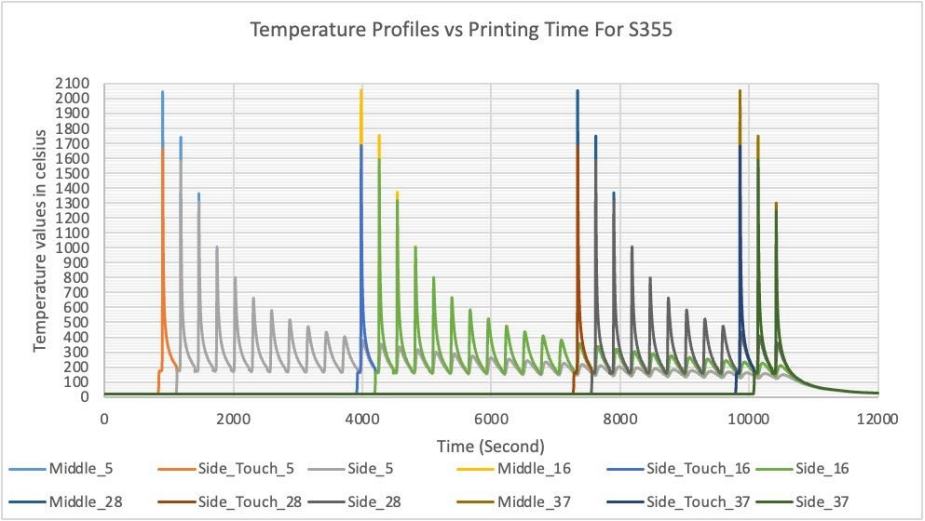

Fig. 10 Temperature history at specific points shown in Fig. 8 for layers 5, 16, 28, and 37 for S355J2G3 low-carbon steel

RESIDUAL STRESSES

The stresses computed during welding simulations rely on the transient temperature histories to calculate the thermal stresses, plastic strains and phase changes. Within any given deposited layer, the stresses become negligible close to the alloy's melt temperature and then begin to increase in magnitude during cooling, resulting in the final residual stress state. Since stress equilibrium must be maintained, regions of high tension are typically balanced with adjacent compressive zones. The longitudinal residual stress, i.e., the stress component coaxial with the direction of weld metal deposition, will be designated as (σ_{xx}), the maximum principal stress (σ_1), and the von Mises stress (σ_v). A quick comparison of the maximum and minimum residual stress magnitudes obtained from 316L builds and low-carbon steel S355J2G3 builds is given in Table 3. These maximum stresses provide some sense of the residual stress magnitudes involved in a WAAM build of a flat plate, but also include local stress concentration effects at reentrant corners. The low-carbon steel has considerably higher magnitude residual stresses. It is interesting to compare the von Mises stress values in the table with the uniaxial room temperature yield stress given in Fig. 5. Not only have both of these alloys yielded in the most highly stressed regions, but also significant strain hardening has occurred to attain some of the high von Mises stress levels given in Table 3.

Table 3 maximum residual stresses for both material models in terms of σ_{XX}, σ_1, σ_V.

Material	Residual stress	Maximum (MPa)	Minimum (MPa)	Range
316L	σ_{xx}	361	-291	652
	σ_1	463	-83	551
	σ_v	389	1.3	387.3
S355J2G3	σ_{xx}	593	-545	1138
	σ_1	593	-208	801
	σ_v	591	1.6	589.4

Fig. 11 contains contour plots of the von Mises residual stresses for both 316L and S355J2G3, using the same reference scale. These ½ symmetry images show the von Mises stresses viewed from the direction of the outermost, air exposed, surface of the plate, in the deformed configuration (exaggerated), after release of the clamp restraints. Though the residual stress magnitudes are different, there are great similarities in the stress contours. It is also recognized that the residual stresses in the base plates are considerably larger for the S355J2G3 material model. It is also noted that close to the top surface of the vertical plate there are significant differences in the residual stress state in the last few layers in comparison with layers lower down in the build. Fig. 12 *a*, *b* shows the σ_{xx} residual stress contours for 316L and S355, on the internal symmetry planes in the respective AM plates after removal of the clamp restraints. In contrast, Fig. 12 *c*, *d* shows the longitudinal stress component from a point of view looking at the opposite surface, i.e., the outermost air exposed surface of the plate. The stress contour plots in Fig. 12 very clearly show the fundamental nature of the residual stress state in the central portion of the WAAM built plates, with high tension along the base, compression in the plate interior mid-level, and then tension close to the top surface. Interestingly, both materials exhibit compressive longitudinal stresses on the topmost surface of the plate.

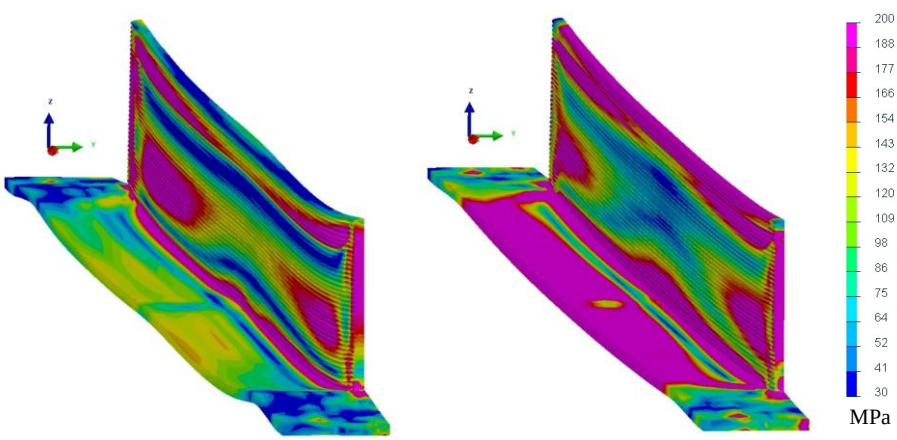

Fig.11 Von Mises residual stress σ_v contour plots: a) 316L stainless steel, b) S355J2G3 low-carbon steel

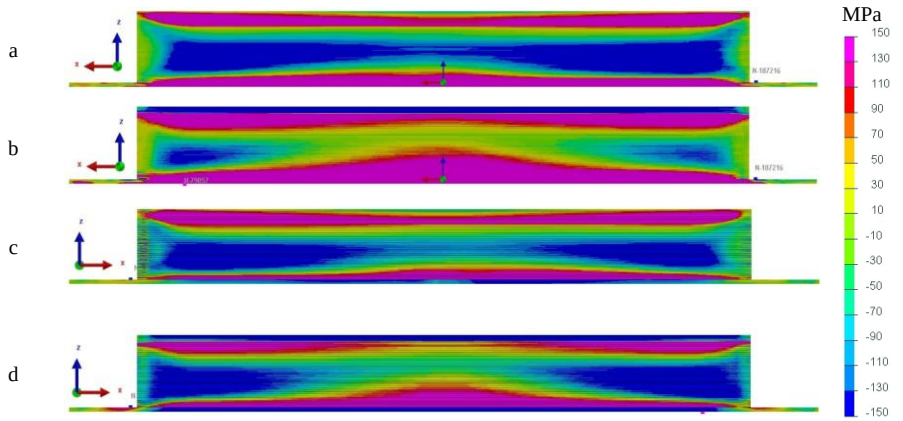

Fig. 12 Longitudinal residual stress σ_{xx}: a) 316L internal symmetry cross section, b) S355 internal symmetry cross section, c) 316L external surface face, d) S355 external surface face

Fig. 13 shows the maximum principal stress contours, σ_1, after unclamping, from the same perspectives used in Fig. 12. The close relationship between the maximum principal stresses and the longitudinal stresses in the central portion of the plates, indicates that the longitudinal stress, σ_{xx}, is the dominant residual stress component in the interior of the plate. Close to the ends of the plate, where σ_{xx} must be zero, the vertical, σ_{zz}, stress component becomes the dominant residual stress, thus forming the "picture frame" residual stress field depicted by the maximum principal stress contours shown in Fig. 13.

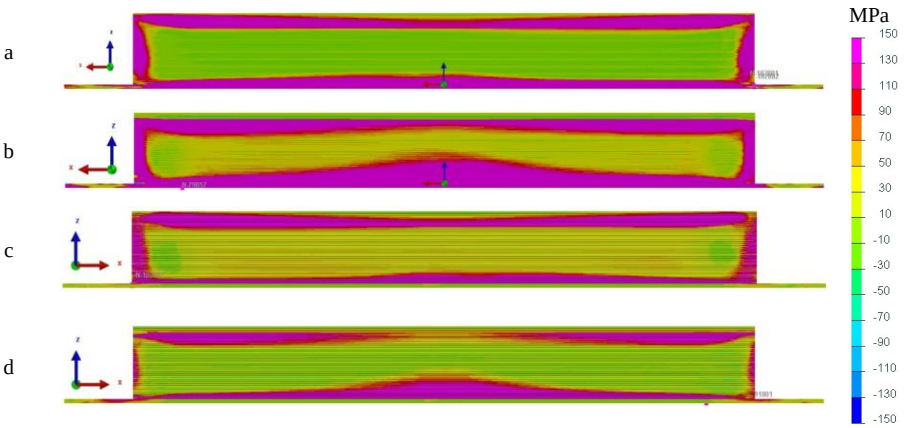

Fig. 13 Maximum principle residual stress σ_1: a) 316L internal symmetry cross section, b) S355 internal symmetry cross section, c) 316L external surface face, d) S355 external surface face

Figs. 11, 12, and 13 depict the final residual stress state after a complex sequence of processing events, where thin hot metal layers are deposited in conjunction with a moving arc weld heat source. Heat transfer effects and clamping restraints play an important role in the evolution of the residual stresses, which after final cooling are obtained following elastic release of the clamping boundary conditions. To better understand how the final residual stresses are obtained, it is instructive to follow the stress evolution as a function of time. Fig. 14 depicts the evolution of the longitudinal stresses, σ_{xx}, and the maximum principal stresses, σ_1, as a function of time during WAAM deposition, workpiece cooling, and final release of clamping restraints. The sequence of images in Fig. 14 show stress contour plots on the exaggerated deformed configuration at times: 280, 2240, 4480, 6720, 8960, 10640, 11500, and 12000 seconds. The first six time intervals correspond to the completion of the deposition of layers 1, 8, 16, 24, 32, and 38. Cooling then starts at 10,640 s, and continues after release of the clamps after 11,500 s. After a small amount of additional cooling (Figs. 9-10), the final residual stresses are shown at 12,000 s. The side-by-side images in Fig. 14 show snapshots of the σ_{xx} and σ_1 stresses for both steel alloy models. One observation is that as the number of printed layers increases, the size of the tensile residual stress zone σ_{xx} (Fig. 14 *a*, *b*), associated with the layers of the most recently deposited metal, moves upwards and maintains an essentially constant vertical dimension. The zone of longitudinal tension is "balanced" by a wide vertical zone of longitudinal compression that continuously increases as the build height increases and the bulk of the metal in the central core region of the plate cools. Thus, in a simplified sense, the residual stress state progresses as a finite width "tension zone" that moves upwards following the vertical motion of the moving heat source as the metal cools. The bulk of the metal in the cooler midsection of the plate is subjected to compressive σ_{xx} stresses, which continuously increases in extent as the AM build continues to cool. Another interesting observation from Fig. 14, is that there always is a difference in the local residual stress state in the last few uppermost layers of deposited metal between 316L and S355J2G3. It is believed that these differences are directly related to the volumetric strains associated with the phase transformations that occur during rapid cooling in the low-carbon steel alloy, S355J2G3.

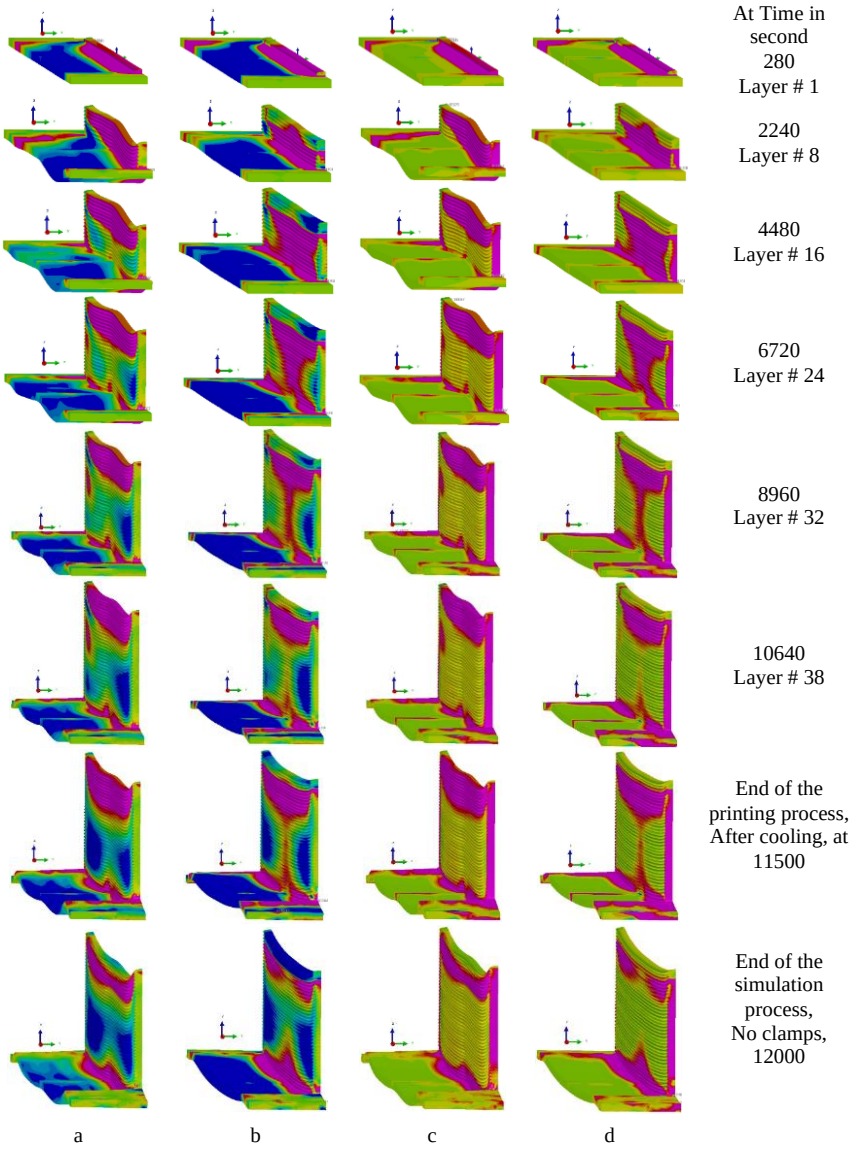

Fig. 14 Residual stress evolution as a function of time: a) σ_{xx} 316L, b) σ_{xx} S355, c) σ_1 316L, d) σ_1 S355

WARPAGE AND DEFORMATION

Fig. 15 shows the vertical displacement (z-direction), for both material models. In general, during a single weld pass, a newly deposited metal layer tends to contract in the longitudinal direction as it cools, resulting in upwards bending of the substrate plate. This overall behavior is exhibited by both material models depicted in Fig. 15 and is consistent with the observed bending deformation shown in the baseplate in the photograph in Fig. 3. The clamping boundary conditions, thickness of the substrate and localized plastic deformation can also affect the final amount of vertical displacement. For example, an increase in thickness of the base substrate will decrease the displacements, but will also increase the magnitude of the σ_{xx} residual stresses.

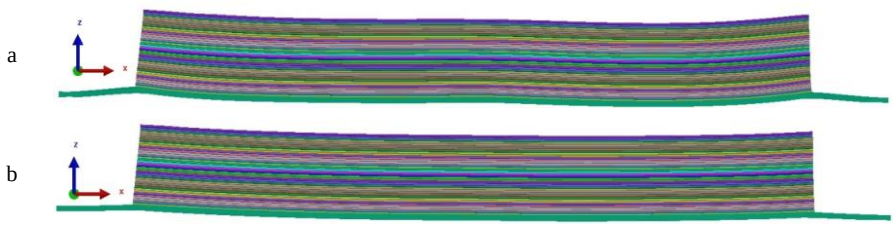

Fig. 15 Deformed (warped) configuration after release from clamp restraints: a) 316L b) S355

Fig. 16 shows the final *z*-displacements, after clamping has been released, for selected layers (5, 16, 28, and 37) as viewed from the vertical symmetry plane. It is immediately noticeable that the 316L material model results in upwards displacements both at the extreme ends of the deposited layers and also on the vertical center line. In contrast, the S355J2G3 material model gives smoothly increasing displacements from the plate's center line out to the edges of the printed plate. The differences in post-weld warping appears to be due to the lower yield stress in 316L and localized plastic deformation that occurs in the base plate while the plate is tightly clamped during the WAAM process. In the 316L model, the greatest *z*-displacement occurs at the starting point of deposition (righthand side of plot in Fig. 16) with a value of 10.39 mm for layer 5. At the symmetry line, the z-displacement is 2.2 mm for this layer, and the *z*-displacement at the end of the line build is 8.2 mm. As can be seen, the *z*-displacements in succeeding layers were essentially identical. For the S355J2G3 low-carbon steel material model, the greatest *z*-displacement value was smaller, 7.73 mm, occurring at the end of the deposition path (lefthand side of Fig. 16), while at the start position on the righthand side of Fig. 16, a *z*-displacement of 6.53 mm was calculated. The displacement difference between the two ends in each layer were almost 2.2 mm for the 316L build and 1.2 mm for the S355J2G3 material model.

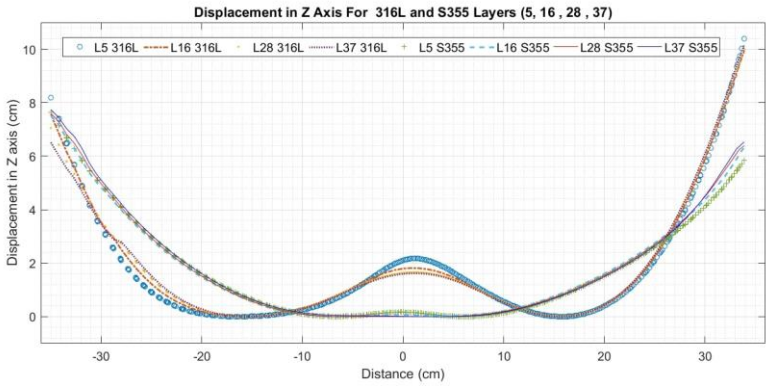

Fig. 16 Comparison of vertical (z-displacements) for 4 discrete layers (5, 16, 28, 37) for 316L and S355

PHASE TRANSFORMATIONS

The primary reason why S355J2G3 low-carbon steel was chosen for direct WAAM comparisons with the austenitic stainless steel, 316L, was to examine the role that phase transformations play in the development of the final residual stresses and material properties. In contrast to austenitic stainless steels, it is well known that low-carbon steels exhibit a variety of phase transformations during heating and cooling. In the SYSWELD simulations, continuous cooling transformation (CCT) diagrams are used to estimate the phase transformation percentages during the rapid cooling associated with welding. Fig. 17 shows the final SYSWELD predicted phase percentages, in the interior of the plate, i.e., on the large vertical plane of symmetry. As shown in this figure, the bulk of the S355J2G3 printed plate is ferrite (Fig. 17a), which is not surprising, since the bulk of the metal is subjected to repeated heating cycles over an extended period of time. A small percentage of martensite is obtained in the final build layers on the top of the plate (Fig. 17 *b*). The last four layers of the build also contain a significant percentage of tempered bainite (Fig. 17*c*), these layers are exposed to low cycle heating for shorter periods of time. As shown in Fig. 17d, a low percentage (~15%) of tempered martensite is also predicted near the end regions of the printed plate. This is due to the different heat transfer conditions and cooling rates that occur near the edges of the plate as compared with the central bulk of the plate.

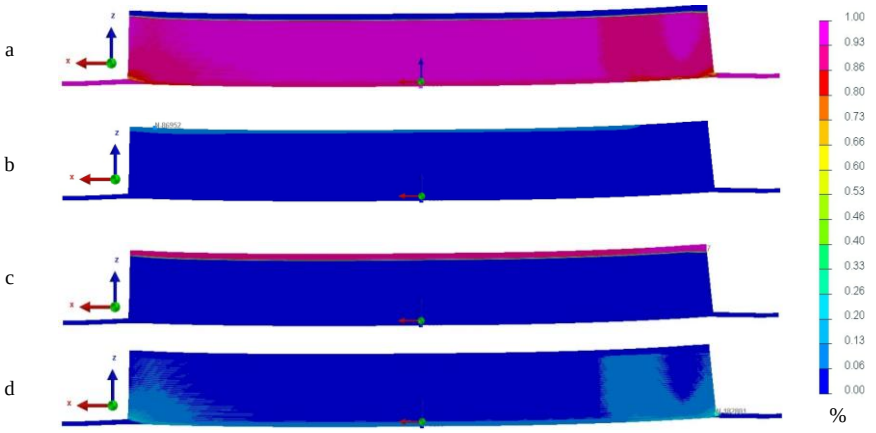

Fig. 17 Post-processing phase percentages and distributions for S355J2G3: a) Ferrite, b) Martensite, c) Tempered Bainite, d) Tempered Martensite

HARDNESS VARIATIONS

Fig. 18 a, b shows the computed hardness results that were obtained from both material models. For the 316L model, in can be seen that for the bulk of the plate, the hardness values are between 150 to 370 (MPa), while in the S355J2G3 printed plate, the predicted range of hardness values is between 370 to 540 (MPa). The last four deposited layers in the S355J2G3 material model predict high hardness values close to the top surface of the plate. This occurs because of the tempered bainite phase transformation as shown in Fig. 17*c*.

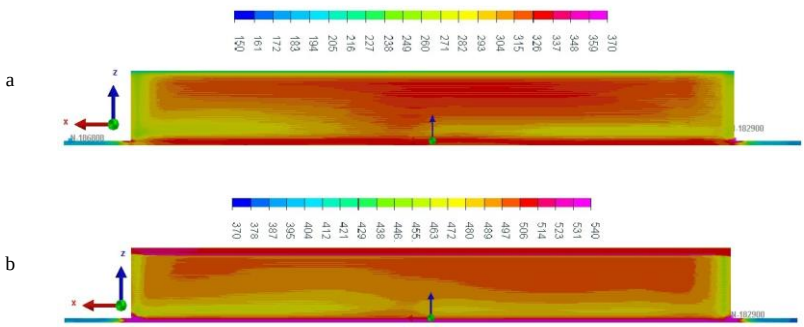

Fig. 18 Predicted hardness variations for: a) 316L b) S355J2G3

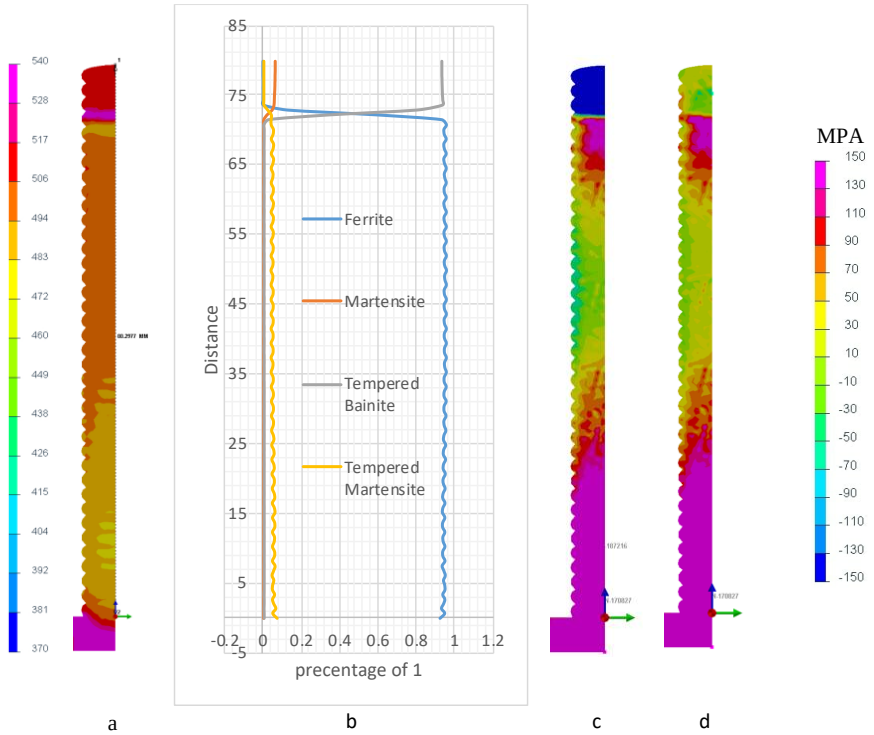

Figure 19 Comparisons in the cross-section plane of the ½-symmetry model for S355J2G3: a) hardness (MPa), b) microstructural phase percentages, c) σ_{xx} stress component, and d) σ_1 maximum principal stress

Fig. 19 (a, b) shows the relationship between the predicted hardness values and the corresponding phase transformation percentages in the ½ symmetry cross-section that is perpendicular to the direction of material deposition in the WAAM S355J2G3 low-carbon steel printed plate. In Fig 19*a* it can be clearly seen how the hardness varies from the bottom to the top of the printed plate and also varies through the thickness of the plate. For example, in the central portion of the plate, the hardness on the exterior surface is higher than on the interior plane of symmetry. The hardness differences through the plate thickness can be attributed to the through thickness thermal gradient, which is directly related to the convective cooling conditions on the plate surface. In Fig. 19 (*c*, d) are the corresponding contour plots for the residual stress components $\sigma_{xx,}$ and the maximum principal stress $\sigma_{1,}$ on the same ½ symmetry cross-section for the S355J2G3 plate. The hardness distribution corresponds to the ratios of the different microstructural phases and the phase transformation percentages, e.g., regions with high percentages of ferrite have relatively low hardness, while regions of the printed plate with high percentages of tempered bainite, have the highest hardness values.

The phase transformations, which introduce differential volumetric strains, also affect the local residual stresses. For example, the σ_{xx} stress component throughout most of the printed plate varies smoothly from tension to relatively low compression. However, where the tempered bainite phase transformation has occurred, e.g., near the top of the

plate, there is a sudden jump to the highly compressive residual stress shown in Fig. 19*c*. Because of the transformation from ferrite to tempered bainite, the microstructural hardness also attains its highest value at this same location. For the 316L material model, there are no phase transformations, and the entire printed plate is austenite. Thus, the residual stresses for 316L are determined solely by the temperature dependent thermomechanical properties of the alloy and generally result in residual stresses that can be evaluated as thermal stresses.

CONCLUSIONS

Two material models were used to simulate the WAAM deposition process using the commercially available finite element software, SYSWELD. The WAAM simulation models were based on two very different types of steel alloys: austenitic stainless steel grade 316L and low-carbon steel S355J2G3. Using a simple, thin plate geometry as an example WAAM printed structure, it was shown that there are a great number of similarities during the evolution of residual stresses and distortion for both of these alloys. For example, even though the heat transfer and metal deposition details are quite complex during WAAM processing, it appears that the resulting residual stress state can be adequately characterized in terms of the maximum principal stresses, in the form of a moving rectangular region of relatively low compression, completely encircled by a rectangular "frame" of high tensile residual stress, as depicted graphically in Fig. 13.

As expected, the S355J2G3 low-carbon steel material model resulted in significantly higher residual stress magnitudes than the austenitic stainless steel 316L However, WAAM simulations for the 316L showed greater welding distortions. This is perhaps not too surprising, since stainless steels generally have relatively high coefficients of thermal expansion and low thermal diffusivity when compared with low-carbon steels. Actual residual stresses and distortions associated with WAAM processing also depend on a relatively large number of controllable parameters, e.g., deposition velocity, heat source energy density, preheating, clamping restraints, deposition path, etc. In this study it has been demonstrated that it is possible to realistically simulate many important physical aspects of the WAAM deposition process using conventional arc welding numerical models. What is not clear is how to best develop numerical simulations for far more complex WAAM geometric builds that might involve many orders of magnitude more weld passes. It is likely that the most effective modeling approach for evaluating much larger WAAM builds in the future will be based on the results obtained from detailed thermomechanical submodels of the sort explored in this study to create much larger global models that do not explicitly model the details associated with every individual weld pass.

References

[1] O. YILMAZ, A.A. UGLA: 'Development of a cold wire-feed additive layer manufacturing system using shaped metal deposition method', *J. Mech. Sci. Technol*, 31, pp. 1611-1620, 2017, doi:10.1007/s12206-017-0308-9.

[2] F. MONTEVECCHI, G. VENTURINI, A. SCIPPA, G. CAMPATELLI: 'Finite Element Modelling of Wire-arc-additive-manufacturing Process', *Procedia CIRP*, 55, pp. 109-114, 2016, doi:10.1016/j.procir.2016.08.024.

[3] VENTURINI, F. MONTEVECCHI, A. SCIPPA, G. CAMPATELLI: 'Optimization of WAAM Deposition Patterns for T-crossing Features', *Procedia CIRP*, 55, 95-100, 2016, doi:10.1016/j.procir.2016.08.043.

[4] D. DING, Z. PAN, D. CUIURI, H. LI: 'Wire-feed additive manufacturing of metal components: technologies, developments and future interests', *Int. J. Adv. Manuf. Technol*, 81, pp. 465-481, 2015. doi:10.1007/s00170-015-7077-3.

[5] C. SHEN, Z. PAN, D. CUIURI, J. ROBERTS, H. LI: 'Fabrication of Fe-FeAl Functionally Graded Material Using the Wire-Arc Additive Manufacturing Process', *Metall. Mater. Trans. B*, 47, pp. 763-772, 2016, doi:10.1007/s11663-015-0509-5.

[6] D. DING, Z. PAN, C. DOMINIC, H. LI: 'Process Planning Strategy for Wire and Arc Additive Manufacturing', in *Robotic Welding, Intelligence and Automation, RWIA 2014, Advances in Intelligent Systems and Computing*, Vol. 363, Springer, Cham., pp. 437-450, 2015, doi.org/10.1007/978-3-319-18997-0_37.

[7] J. RUAN, T.E. SPARKS, Z. FAN, J.K. STROBLE, A. PANACKAL: 'A Review of Layer Based Manufacturing Processes for Metals', *Proceedings of the 17th Annual Solid Freeform Fabrication Symposium (2006, Austin, TX)*, pp. 233-245, 2006, doi.org/10.26153/tsw/7133.

[8] Z. PAN, D. DING, B. WU, D. CUIURI: 'Arc Welding Processes for Additive Manufacturing: A Review', *Transactions on intelligent welding manufacturing*, pp. 3-24, 2018, doi:10.1007/978-981-10-5355-9.

[9] H. GENG, J. XIONG, D. HUANG, X. LIN, J. LI: 'A prediction model of layer geometrical size in wire and arc additive manufacture using response surface methodology', *Int. J. Adv. Manuf. Technol*, 93, pp. 175-186, 2017, doi:10.1007/s00170-015-8147-2.

[10] B.A. SZOST, S. TERZI, F. MARTINA, D. BOISSELIER, A. PRYTULIAK, T. PIRLING, M. HOFMANN, D.J. JARVIS: 'A comparative study of additive manufacturing techniques: Residual stress and microstructural analysis of CLAD and WAAM printed Ti-6Al-4V components', *Mater. Des*, 89, pp. 559-567, 2016, doi:10.1016/j.matdes.2015.09.115.

[11] A. BUSACHI, J. ERKOYUNCU, P. COLEGROVE, F. MARTINA, J. DING: 'Designing a WAAM based manufacturing system for defence applications', *Procedia CIRP*, 37, pp. 48-53, 2015, doi:10.1016/j.procir.2015.08.085.

[12] S.W. WILLIAMS, F. MARTINA, A.C. ADDISON, J. DING, G. PARDAL, P. COLEGROVE: 'Wire + Arc Additive Manufacturing', *Mater. Sci. Technol*, 32, pp. 641-647, 2016, doi:10.1179/1743284715Y.0000000073.

[13] J.Y. BAI, C.L. YANG, S.B. LIN, B.L. DONG, C.L. FAN: 'Mechanical properties of 2219-Al components produced by additive manufacturing with TIG', *Int. J. Adv. Manuf. Technol*, 86, pp. 479-485, 2016, doi:10.1007/s00170-015-8168-x.

[14] S. SURYAKUMAR, K.P. KARUNAKARAN, U. CHANDRASEKHAR, M.A. SOMASHEKARA: 'A study of the mechanical properties of objects built through weld-deposition', *Proc. Inst. Mech. Eng., Part B: J. Eng. Manuf.*, 227(8), pp. 1138-1147, 2013, doi:10.1177/0954405413482122.

[15] C. V. HADEN, G. ZENG, F.M. CARTER, C. RUHL, B.A. KRICK, D.G. HARLOW: 'Wire and arc additive manufactured steel: Tensile and wear properties', *Addit. Manuf.*, 16, pp. 115-123, 2017, doi:10.1016/j.addma.2017.05.010.

[16] N.W. KLINGBEIL, J.L. BEUTH, R.K. CHIN, C.H. AMON: 'Residual stress-induced warping in direct metal solid freeform fabrication', *Int. J. Mech. Sci*., 44, pp. 57-77, 2002, doi:10.1016/S0020-7403(01)00084-4.

[17] E.R. DENLINGER, J.C. HEIGEL, P. MICHALERIS, T.A. PALMER: 'Effect of inter-layer dwell time on distortion and residual stress in additive manufacturing of titanium and nickel alloys', *J. Mater. Process. Technol*., 215, pp. 123-131, 2015, doi:10.1016/j.jmatprotec.2014.07.030.

[18] X. BAI, H. ZHANG, G. WANG: 'Modeling of the moving induction heating used as secondary heat source in weld-based additive manufacturing', *Int. J. Adv. Manuf. Technol*., 77 pp. 717-727, 2015, doi:10.1007/s00170-014-6475-2.

[19] P.A. COLEGROVE, H.E. COULES, J. FAIRMAN, F. MARTINA, T. KASHOOB, H. MAMASH, L.D. COZZOLINO: 'Microstructure and residual stress improvement in wire and arc additively manufactured parts through high-pressure rolling', J. *Mater. Process. Technol*., 213, pp. 1782-1791, 2013, doi:10.1016/j.jmatprotec.2013.04.012.

[20] A.H. NICKEL, D.M. BARNETT, F.B. PRINZ: 'Thermal stresses and deposition patterns in layered manufacturing', *Mater. Sci. Eng. A*., 317, pp. 59-64, 2001, doi:10.1016/S0921-5093(01)01179-0.

[21] H. ZHAO, G. ZHANG, Z. YIN, L. WU: 'A 3D dynamic analysis of thermal behavior during single-pass multi-layer weld-based rapid prototyping', *J. Mater. Process. Technol*., 211(3), pp. 488-495, 2011, doi:10.1016/j.jmatprotec.2010.11.002.

[22] H. ZHAO, G. ZHANG, Z. YIN, L. WU: 'Three-dimensional finite element analysis of thermal stress in single-pass multi-layer weld-based rapid prototyping', *J. Mater. Process. Technol*., 212, pp. 276-285, 2012, doi:10.1016/j.jmatprotec.2011.09.012.

[23] SYSWELD 2021.0 – Documentation Package, ESI North America, Farmington Hills, MI.

[24] W. WORLD, L.E. SOUDAGE, D. LE, T. GUWAHATI, T. BOMBAY: 'Efficient estimation of volumetric heat source in fusion welding process simulation', in *Fusion Welding Process Simulation*, 56, pp. 88-97, 2013, doi:10.1007/BF03321399.

[25] M.P. MUGHAL, H. FAWAD, R.A. MUFTI: 'Three-dimensional finite-element modelling of deformation in weld-based rapid prototyping', *Proc. Inst. Mech. Eng., Part C: J. Mech. Eng. Sci*., 220(6), pp. 875-885, 2006, doi:10.1243/09544062JMES164.

[26] DING, P. COLEGROVE, J. MEHNEN, S. GANGULY, P.M.S. ALMEIDA, F. WANG, S. WILLIAMS: 'Thermo-mechanical analysis of Wire and Arc Additive Layer Manufacturing process on large multi-layer parts', *Comput. Mater. Sci.*, 50, pp. 3315-3322, 2011, doi:10.1016/j.commatsci.2011.06.023.

[27] T. KIK, M. SLOVACEK, J. MORAVEC, M. VANEK: 'Numerical Simulations of Heat Treatment Processes', *Appl. Mech. Mater, Trans Tech Publications*, Vol. 809-810, pp. 799-804, 2015, doi:10.4028/www.scientific.net/AMM.809-810.799.

[28] J.V. GORDON, C.V. HADEN, H.F. NIED, R.P. VINCI, D.G. HARLOW: 'Fatigue crack growth anisotropy, texture and residual stress in austenitic steel made by wire and arc additive manufacturing', *Mater. Sci. Eng. A*., 724, pp. 431-438, 2018, doi:10.1016/j.msea.2018.03.075.